

A Multi-Static Ground-Penetrating Radar with an Array of Resistively-Loaded Vee Dipole Antennas for Landmine Detection

Kangwook Kim, Ali Cafer Gurbuz, Waymond R. Scott, Jr., and James H. McClellan

School of Electrical and Computer Engineering
Georgia Institute of Technology
Atlanta, GA 30332-0250

ABSTRACT

A multi-static ground-penetrating radar (GPR) has been developed to investigate the potential of multi-static inversion algorithms. The GPR consists of a linear array of six resistively-loaded vee dipoles (RVDs), a network analyzer, and a microwave switch matrix all under computer control. The antennas in the array are spaced 12 cm apart so the spacing between the transmitter and the receiver pairs in the measurements are from 12 cm to 96 cm in 12 cm increments. The size of the array is suitable for the landmine problem and scaled measurements of the buried structure problem. The RVD is chosen as an array element because it is very "clean" in that it has very little self clutter and a very low radar cross section to lessen the reflections between the ground and the antenna. The shape and the loading profile of the antenna are designed to decrease the reflection at the drive point of the antenna while increasing the forward gain. The antenna and balun are made in a module, which is mechanically reliable without significant performance degradation. The multi-static GPR operation is demonstrated on targets buried in clean sand and targets buried under the ground covered by rocks. The responses of the targets are measured by each transmitter-receiver pair. A synthetic aperture, multi-static GPR imaging algorithm is extended from conventional monostatic back-projection techniques and used to process the data. Initial images obtained from the multi-static data are clearer than those obtained from bistatic data.

Keywords: Ground-penetrating radar (GPR), landmine detection, resistively-loaded vee dipole (RVD), multi-static imaging, back-projection

1. INTRODUCTION

Multi-static ground-penetrating radar (GPR) uses an array of antennas to conduct a number of bistatic operations simultaneously. A multi-static GPR is used to obtain more information on the target of interest using angular diversity. With an appropriate multi-static inversion algorithm, a multi-static GPR may perform better than typical bistatic GPR. A multi-static GPR system has been developed to investigate the potential of multi-static inversion algorithms.¹ The targets of interest in this paper are near-surface man-made objects, such as landmines.

The resistively-loaded vee dipole (RVD) is chosen as an array element. The RVD is typically a vee dipole, whose arms are continuously loaded with the Wu-King resistive profile.²⁻⁴ The RVD in this paper has curved arms, and the arms are loaded with chip resistors according to a modified Wu-King profile.⁵⁻⁸ The RVD is packaged appropriately so that the mechanical reliability is enhanced while maintaining its radiation characteristics.⁹ The RVD is suitable for the multi-static GPR application because its form allows the antennas to be closely spaced in the array. It radiates a very clean and compact pulse because the resistive profile suppresses most of the self clutter. It has a very low radar cross section to lessen the reflection between the ground and the antenna.

Further author information: (Send correspondence to K. Kim)

K. Kim: E-mail: kangwook.kim@ece.gatech.edu, Telephone: 404-894-3123

A. C. Gurbuz: E-mail: alicafaer@ece.gatech.edu, Telephone: 404-894-2977

W. R. Scott: E-mail: waymond.scott@ece.gatech.edu, Telephone: 404-894-3048

J. H. McClellan: E-mail: jim.mcclellan@ece.gatech.edu, Telephone: 404-894-8325

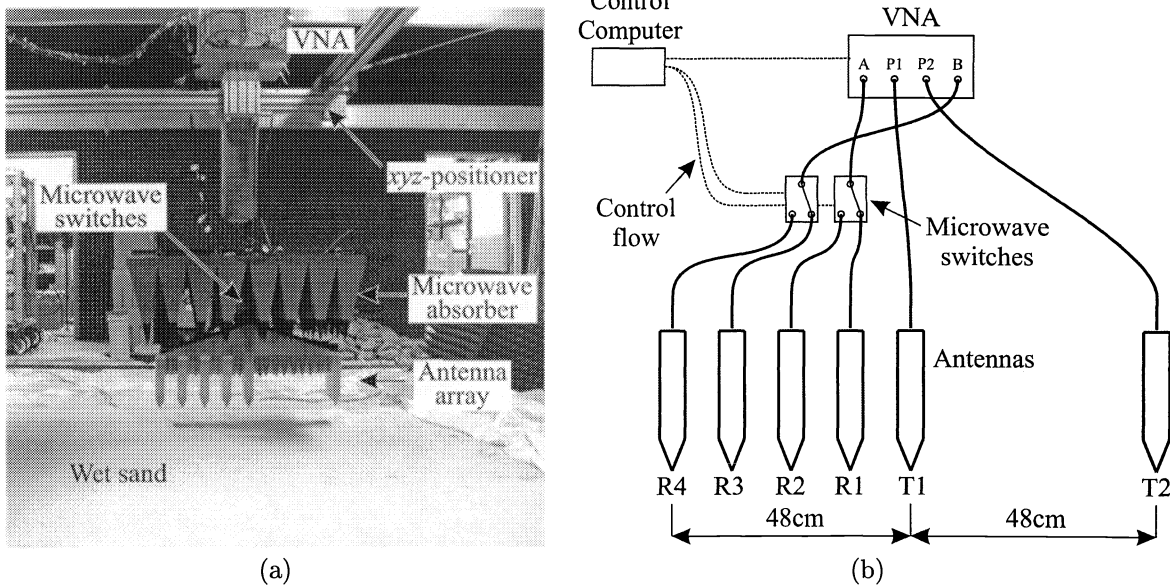


Figure 1. (a) Photograph of the multi-static GPR (control computer not shown) and (b) its diagram.

Currently, most inversion algorithms for bistatic GPR work either in the time domain or in the frequency domain. The delay-sum back-projection algorithm is an example of the time-domain inversion algorithm.¹⁰ The biggest advantage of this type of algorithm may be its flexibility. It is not demanding to modify the algorithm to take into account the transmitter-receiver spacing. However, it is computationally intensive. The ω - k migration algorithm is an example of the frequency domain algorithm.^{11,12} It is much faster than the delay-sum back-projection algorithm. However, the transmitter-receiver spacing is not generally considered in implementing the ω - k migration algorithm. In this paper, we modify the delay-sum back-projection algorithm to invert the multi-static GPR data. The algorithm is modified to include the transmitter-receiver spacing, which is very important because the GPR works very close to the target in this paper: the transmitter-receiver spacing is larger than the target distance to the antenna array.

In Section 2, the hardware configuration of the multi-static GPR is described. As examples of possible apertures for multi-static inversion algorithms, two methods of synthesizing multi-static apertures are illustrated. In Section 3, the operation of the multi-static GPR is demonstrated on targets buried in clean sand and targets buried in cluttered sand. In Section 4, the modified delay-sum back-projection algorithm is described and operated on the landmine targets.

2. MULTI-STATIC GROUND-PENETRATING RADAR

The multi-static GPR in this paper consists of a linear antenna array, a vector network analyzer (Agilent 8720D), two microwave switches, and a control computer. The picture and diagram of the system are shown in Figure 1. The antenna array consists of six identical antennas: two transmitters, T1 and T2, and four receivers, R1, R2, R3, and R4. Transmitters T1 and T2 are directly connected to ports P1 and P2 of the network analyzer, respectively, receivers R1 and R2 are connected to sampler A of the network analyzer through a microwave switch, and receivers R3 and R4 are connected to sampler B of the network analyzer through another microwave switch. The antenna array is housed in a dielectric frame. To reduce the reflections from the array frame and coaxial cables running behind the frame, microwave absorber is used to pad in the areas between the antenna elements and wrap the coaxial cables. To further reduce the reflections from the positioner, which is mostly caused by the wave reflected from the ground, 45.7 cm high pyramidal microwave absorber is placed behind the array frame.

The analyzer has a single source and two samplers.¹³ The activation of T1 and T2 are determined according to the state of the internal switch. The two samplers can operate simultaneously. By using two external microwave

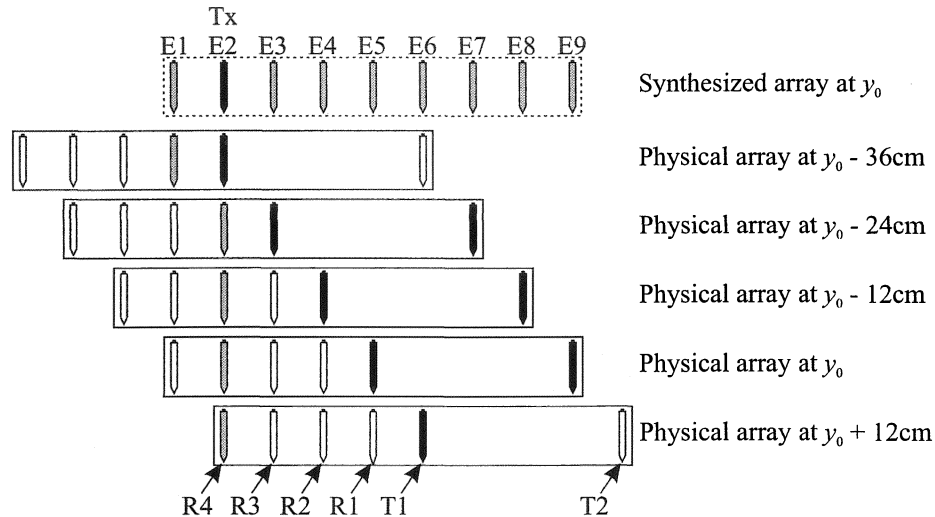


Figure 2. Diagram of the synthesis procedure for the 96 cm wide, nine-element synthetic array aperture when element E2 behaves as a transmitter.

switches, the signals from R1 and R3 can be measured at a time and signals from R2 and R4 can be measured at the next time. The operations of the analyzer, internal switch, and external switches are all controlled by a personal computer, which is equipped with National Instrument LabView software. The control computer also controls the xyz -positioner, which moves the antenna array over the sand.

The spacing between the antenna elements is 12 cm, except for the spacing between the transmitters, which is 48 cm. We can obtain eight elementary bistatic apertures from the array: 12 cm, 24 cm, 36 cm, and 48 cm wide apertures from T1-R1, T1-R2, T1-R3, and T1-R4 pairs, respectively, when T1 is activated, and 60 cm, 72 cm, 84 cm, 96 cm wide apertures from T2-R1, T2-R2, T2-R3, and T2-R4 pairs, respectively, when T2 is activated. Other than the elementary bistatic apertures, we can obtain various synthetic array apertures by using the reciprocity and synthesizing the measurements at different locations. Two example formations are illustrated here. One example is the formation of 96 cm wide, nine-element array aperture, where all the elements behave both as a transmitter and receiver. The other example is the formation of 196cm wide, 17-element array aperture, where only the center element behaves as a transmitter and the other elements behave as receivers.

The synthesis of the 96 cm wide, nine-element array aperture requires measurements at up to five locations, depending on which element behaves as a transmitter. As an example, the formation of the synthetic array when the second element from the left behaves as a transmitter is illustrated in Figure 2. In the figure, the array shown on the top is the synthesized array, in which element E2 behaves as a transmitter and the other eight elements behave as receivers. The figure also shows the locations of the physical array and the elements to be activated to synthesize the aperture shown on the top. Here, we assume that both the array orientation and the scan path are along the y -axis. The synthesized array is assumed to be centered at y_0 . To obtain the synthesized response from element E1, we center the physical array at $y_0 - 36$ cm, activate T1, and measure the response from R1. To obtain the synthesized response from element E3, we center the physical array at $y_0 - 24$ cm, activate T1, and measure the response from R1. Note that in this configuration, physical transmitter T1 is at the position of the synthesized receiver E3, and physical receiver R1 is at the position of the synthesized transmitter E2. The roles of the transmitter and the receiver can be switched using the principle of reciprocity. Using the same principle, we can obtain the synthesized response from E7 by activating T2 and measuring the response from R1. Similarly, the synthesized responses from E4 and E8 can be obtained by centering the physical array at $y_0 - 12$ cm and measuring bistatic responses from T1-R2 and T2-R2, respectively. The synthesized response from E5 and E9 can be obtained by centering the physical array at y_0 and measuring bistatic responses from T1-R3 and T2-R3, respectively. Finally, the synthesized response from E5 can be obtained by centering the physical array at $y_0 + 12$ cm and measuring bistatic response from T1-R4. Similarly, we can obtain the synthesized array aperture when another element behaves as a transmitter. Note that this synthesis procedure requires the physical

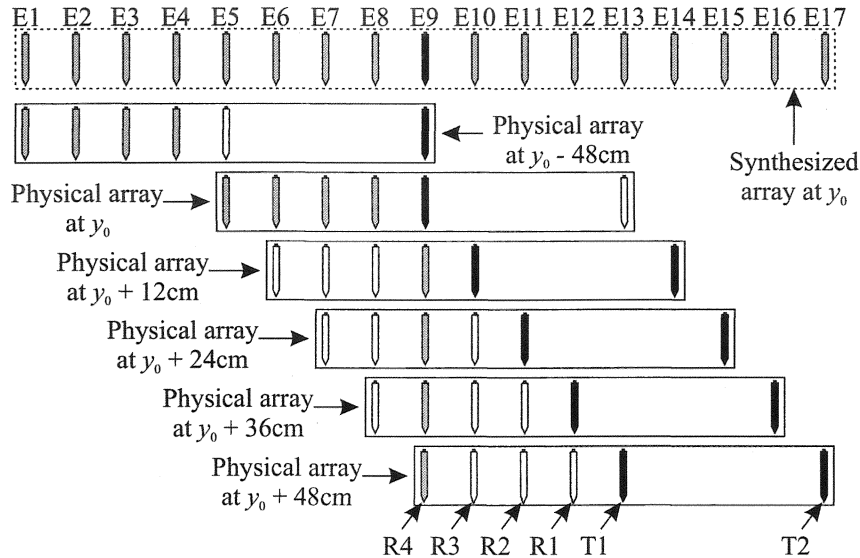


Figure 3. Diagram of the synthesis procedure for the 196 cm wide, 17-element synthetic array aperture.

array to pass only once along a linear scan path. The physical array stops at each 12 cm increment along the scan path, and all the elementary bistatic responses are recorded. The synthesis is performed after the measurement.

Figure 3 illustrates the formation of the 196 cm wide, 17-element synthetic array aperture. The array shown on the top is the synthesized array. In this array, only the center element E9 behaves as a transmitter, and all the other elements behave as receivers. The figure also shows the locations of the physical array and the elements to be activated to synthesize the aperture shown on the top. Again, we assume that both the array orientation and the scan path are along the y -axis. Similarly to the procedure for the nine-element synthetic array, the synthesized responses for the 17-element synthetic array at y_0 are obtained by using scans at $y_0 - 48$ cm, y_0 , $y_0 + 12$ cm, $y_0 + 24$ cm, $y_0 + 36$ cm, and $y_0 + 48$ cm and using the principle of reciprocity.

3. MULTI-STATIC EXPERIMENTS

The multi-static GPR is used to obtain responses from landmine targets buried in sand with clean surface and in sand with cluttered surface (Figure 4). The targets are buried according to the burial map shown in Figure 5 (b) at depths ranging from 1.0 cm to 11.5 cm where the buried depth of a target is measured from the surface of the sand to the top of the target. The targets in these experiments are anti-tank mines, i.e., VS-1.6, VS-2.2, and TMA-5, anti-personnel mines, i.e., TS-50, mine simulant, PFM-1, and M-14, and four clutter objects, i.e., 5.08 cm-diameter metal sphere, rock, crushed aluminum can, and nylon cylinder. The picture of the targets is shown in Figure 5 (a), and the properties of the targets are summarized in Table 1. In the clean-surface experiment, the surface of the sand is packed and flattened. The surface height varies by 2 cm at most. In the cluttered experiment, river rocks of various sizes and shapes are laid on the flat surface. The spacing between the rocks is chosen empirically to maximize the clutter effect.

The antennas are elevated by 10 cm from the surface of the sand and scanned over $1.8\text{ m} \times 1.8\text{ m}$ region. Each point on the surface of the scan region is defined by x - and y -coordinates, both of which range from -90 cm to 90 cm. The origin of the coordinates is located in the center of the scan area. The location of the antenna array is determined by the center point of the array. The array scans over lines along the y -direction, which are equally spaced from $x = -90$ cm to 90 cm with 2 cm increment. The array stops at 91 points with 2 cm increment as it moves along each line. At each stop, the network analyzer measures the responses from the eight elementary bistatic pairs at 401 equally-spaced frequency points from 60 MHz to 8.06 GHz, and the frequency-domain response is recorded. The responses in the frequency domain are transformed into the time domain for

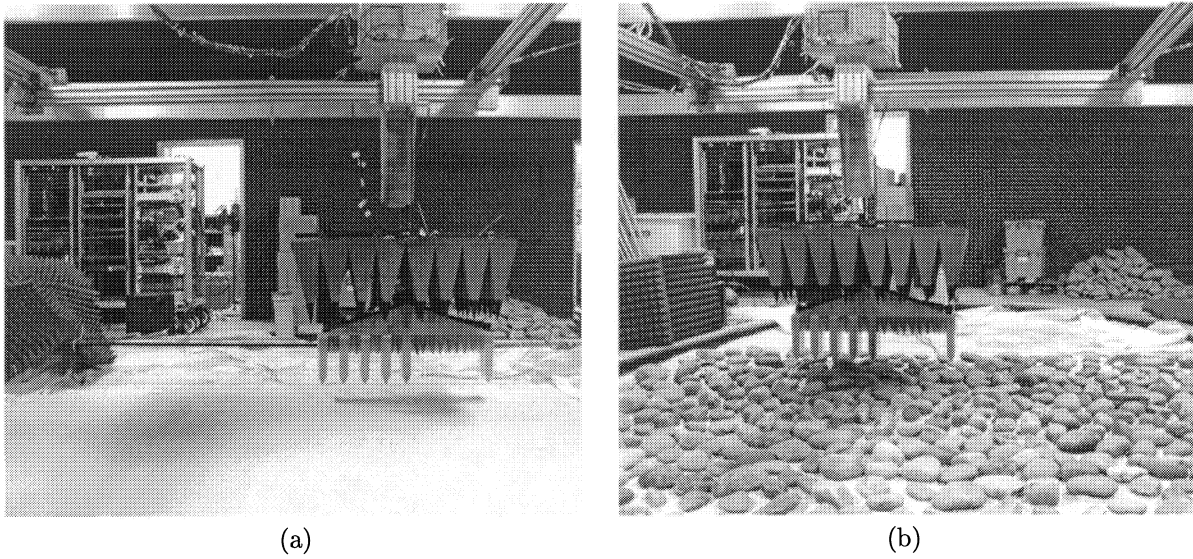


Figure 4. Pictures of the experiment setup for (a) targets buried in sand with clean surface and (b) targets buried in sand with cluttered surface.

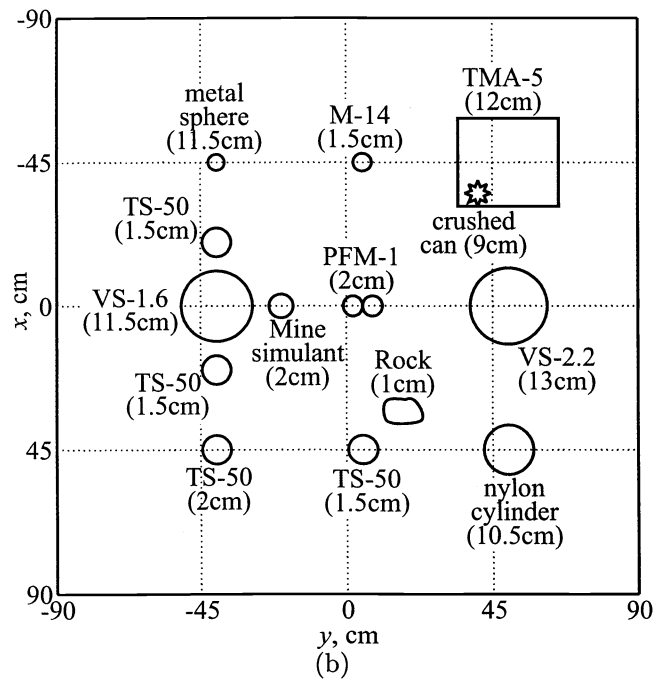
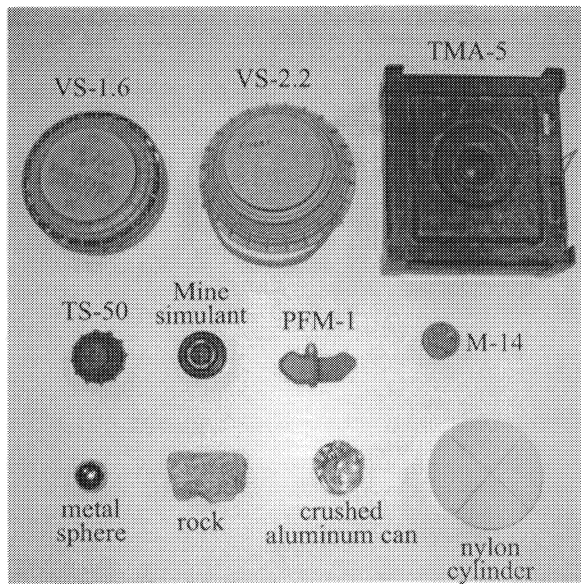


Figure 5. (a) Picture of the buried targets and (b) burial map of the targets in sand. The numbers in the parentheses are the buried depths of the targets.

Table 1. Summary of Target Properties. In the dimensions column, L, W, D, and H represent length, width, diameter, and height, respectively. The target dimensions are shown in centimeters.

target	type	material	dimensions (cm)
VS-1.6	anti-tank	plastic	22.2 (D), 9.2 (H)
VS-2.2	anti-tank	plastic	24.0 (D), 12.0 (H)
TMA-5	anti-tank	plastic	31.2 (L), 27.5 (W), 11.3 (H)
TS-50	anti-personnel	plastic	9.0 (D), 4.5 (H)
PFM-1	anti-personnel	plastic	11.9 (L), 6.4 (W), 2.0 (H)
M-14	anti-personnel	plastic	5.6 (D), 4.0 (H)
mine simulant	simulant	plastic	7.5 (D), 3.8 (H)
metal sphere	clutter	aluminum	5.1 (D)
rock	clutter	rock	12.0 (L), 8.0 (W), 7.5 (H)
crushed coke can	clutter	aluminum	8.0 (D), 3.0 (H)
nylon cylinder	clutter	nylon	15.5 (D), 7.6 (H)

an input differentiated Gaussian pulse, which is represented as

$$v(t) = V_0 \frac{t}{\tau} e^{0.5-2(t/\tau)^2}, \quad f_{pk} = \frac{1}{\pi\tau} \quad (1)$$

where V_0 is the peak-to-peak amplitude, τ is the peak-to-peak interval, and f_{pk} is the peak frequency. In this paper, $f_{pk} = 2.5$ GHz is used to process the images.

Figure 6 shows the gray-scale graphs of the signal intensities obtained from four elementary bistatic apertures, i.e., T1-R1, T1-R3, T2-R2, and T2-R4. The figure shows the response of the GPR along the line at $x = 0$, which goes over VS-1.6, mine simulant, PFM-1, and VS-2.2. The graphs on the left column are those from the clean surface experiment, and the graphs on the right column are those from the cluttered surface experiment. In each graph, the horizontal axis represents the y -coordinates of the antenna array, and the vertical axis represent the signal return time. These graphs are obtained by transforming the bistatic responses in the frequency domain into the time domain to give the response to a differentiated Gaussian pulse with a center frequency of 2.5 GHz. The graphs are shown on a 40 dB scale.

Figure 7 shows the gray-scale graphs obtained in a similar manner to Figure 6. It shows the responses of targets along the line at $y = -40$ cm, which are the metal sphere, VS-1.5, and three TS-50's. The antenna array is located over the lines at $y = -34$ cm, -22 cm, -52 cm, and -40 cm for the graphs obtained from T1-R1, T1-R3, T2-R2, and T2-R4 bistatic pairs, respectively, whose centers all go over the line at $y = -40$ cm. The horizontal axis represents the x -coordinates of the antenna array.

In Figures 6 and 7, the reflections from the surface of the sand are seen near 1.9 nsec, 2.2 nsec, 3.0 nsec, and 3.7 nsec for T1-R1, T1-R3, T2-R2, and T2-R4 bistatic pairs, respectively. The intensities of the signals from both the surface of the sand and the targets are weaker for the wider bistatic apertures because of the longer path lengths and the directional characteristic of the antenna elements. In the cluttered surface experiment, the responses are heavily cluttered. The clutter obscures the responses of the targets, especially those of the shallow targets. The hyperbolic responses of the targets are hardly seen. The clutter effects are mostly due to the distortion of the wave front, the reflections inside the rocks, and the reflections between the rocks. Note that, based on the burial depths of the targets and the gray-scale graphs obtained from the T1-R1 bistatic pairs, the speed of the electromagnetic wave propagation in sand is estimated to be roughly 0.4 times that in free space.

4. MODIFIED DELAY-SUM BACK-PROJECTION

When an antenna is scanned over a region, the target response is of a hyperbolic curve. The typical delay-sum back-projection (DSBP) algorithm implements matched filtering as a coherent summation along the hyperbolic

curve for every pixel in the image, which may be represented as¹⁴:

$$f(y_T, z_T) = \int_{-\infty}^{\infty} \int_{-\infty}^{\infty} w(y_T - u) d(u, t) \delta\left(t - \frac{c}{2} \sqrt{(y_T - u)^2 + z_T^2}\right) dt du, \quad (2)$$

where $d(u, t)$ is the measured monostatic response in the space-time domain, $f(y_T, z_T)$ is the intensity of the back-projected image at position (y_T, z_T) , and $w(u)$ is the aperture weight function. Equation (2) is based on

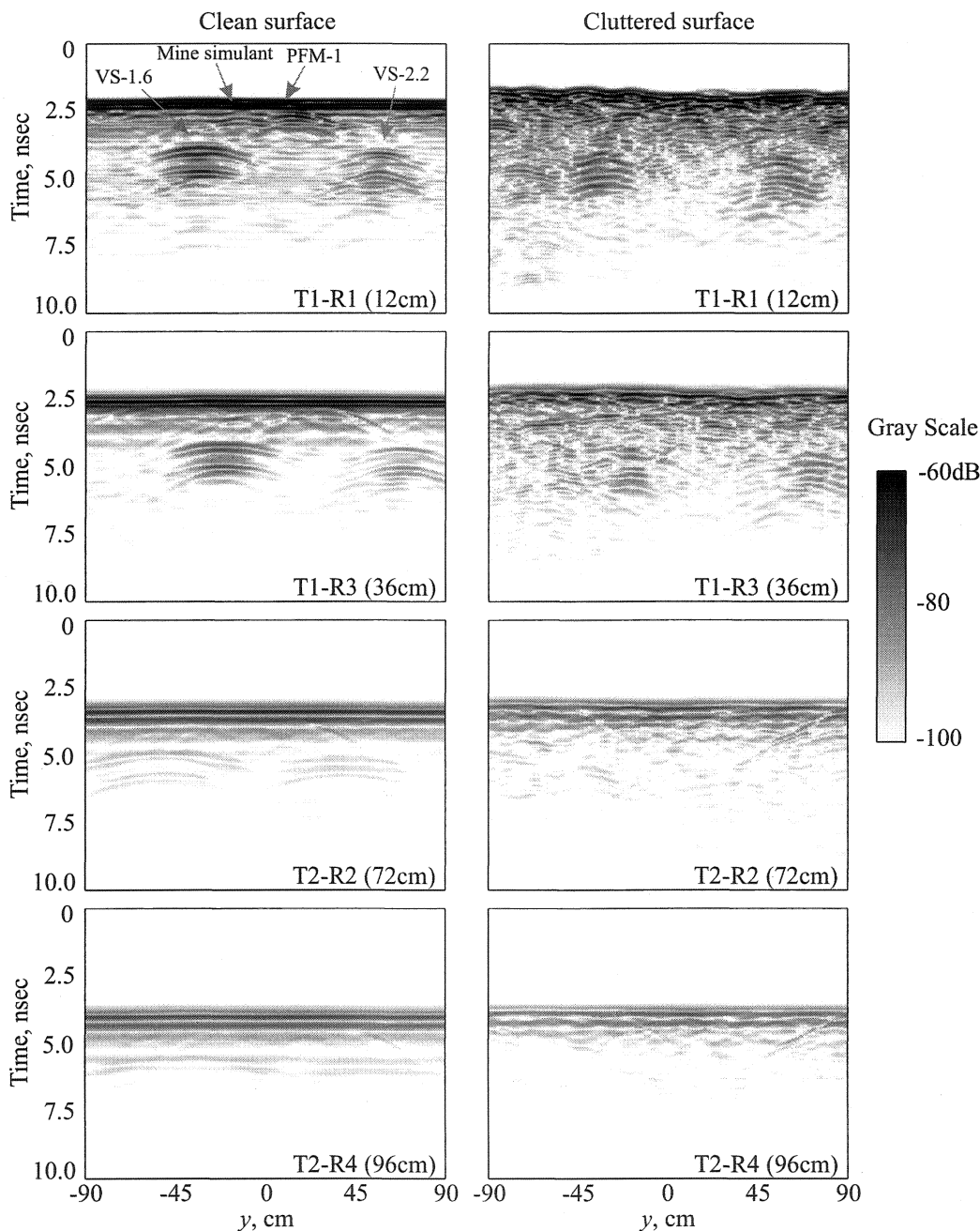


Figure 6. Gray-scale graphs of the signal intensities obtained from 12 cm, 36 cm, 72 cm, and 96 cm wide bistatic apertures when the array is scanned over the line at $x = 0$. The graphs on the left column are those from the clean surface experiment, and the graphs on the right column are those from the cluttered surface experiment.

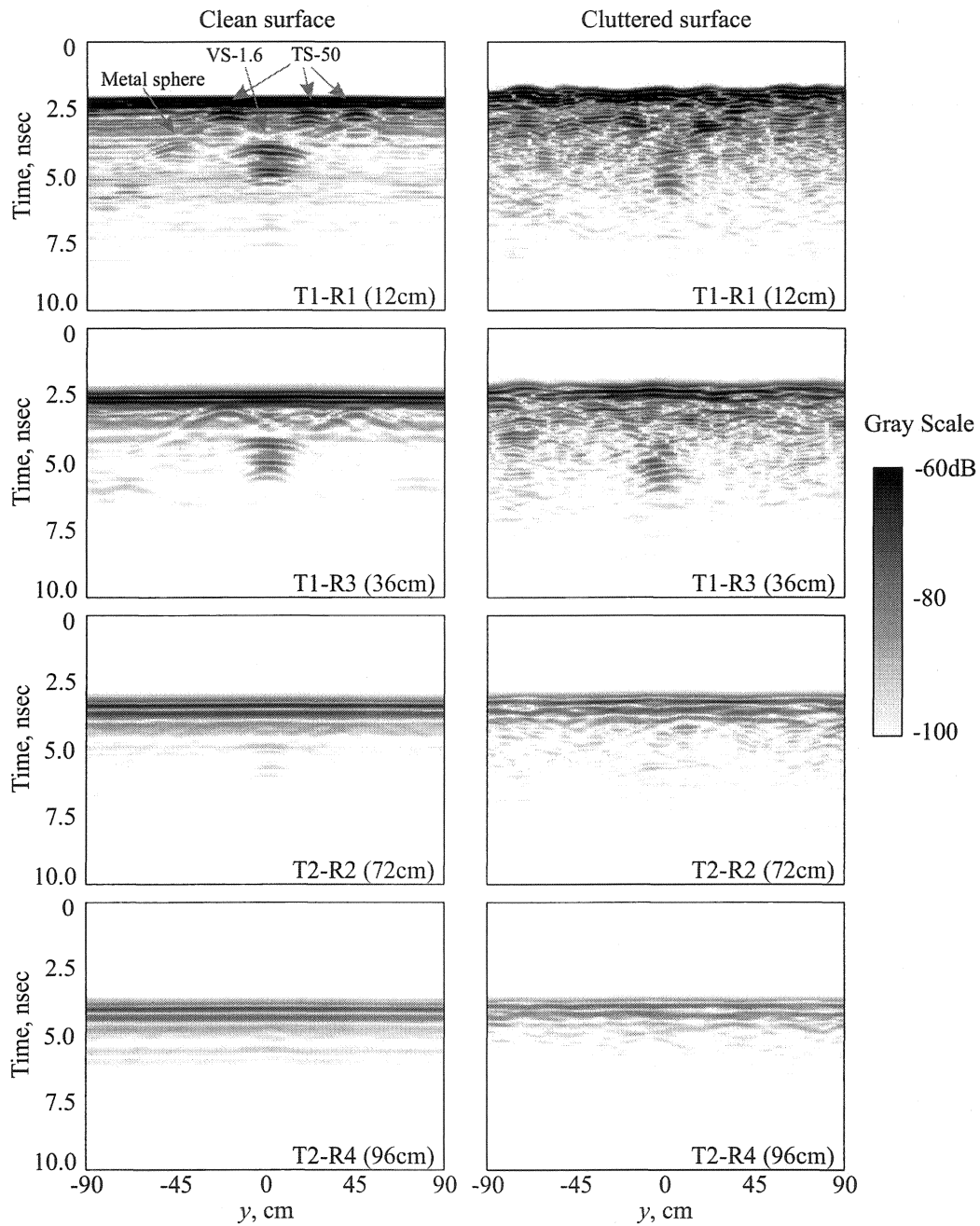


Figure 7. Gray-scale graphs of the signal intensities obtained from 12 cm, 36 cm, 72 cm, and 96 cm wide bistatic apertures when the centers of the bistatic apertures move over the line at $y = -40$ cm. The graphs on the left column are those from the clean surface experiment, and the graphs on right column are those from the cluttered surface experiment.

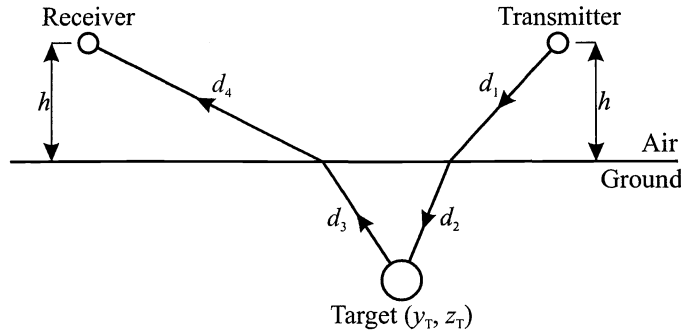


Figure 8. Diagram of the wave path in geometrical optics sense.

two assumptions: first, the transmitter-receiver spacing is assumed to be zero, and, second, radar and the target are assumed to be in a homogeneous medium. These assumptions cannot be used in the multi-static GPR in this paper for the following reasons. First, the distance between the antenna and the target are smaller than the size of the antenna array. Second, the radar and the targets are in different media: air and sand.

To take the transmitter-receiver spacing and air-sand interface, consider the typical situation shown in Figure 8. The figure shows the wave path from a transmitter to a receiver in geometrical optics sense, which is used to determine the delay of the signal. Note that the wave is refracted at the air-sand interface. The refraction point can be obtained from the Snell's law. In this case, the modified DSBP algorithm can be represented as:

$$f(y_T, z_T) = \int_{-\infty}^{\infty} \int_{-\infty}^{\infty} w(y_T - u) d(u, t) \delta \left(t - \left[\frac{d_1 + d_4}{c} + \frac{d_2 + d_3}{v} \right] \right) dt du, \quad (3)$$

where d_1 , d_2 , d_3 , and d_4 are wave path lengths, c is the wave velocity in air, and v is the wave velocity in sand.

Figure 9 shows the preliminary back-projected images obtained using the modified DSBP algorithm. The figure shows the back-projected images of Figure 6. To obtain these images, a ground-reflection technique is used before the DSBP algorithm is applied. We generated a ground-reflection model for each bistatic aperture by averaging responses of the scan region when no target is present. The ground-reflection model is correlated with the bistatic response at each measurement point to determine the lag. An appropriately delayed version of the model is then subtracted from the measurement. The modified DSBP algorithm is then applied to the ground-reflection removed images. Here, the speed of wave propagation is assumed to be 1.5×10^8 m/sec, the solution to the Snell's law is approximated to speed up the algorithm,¹⁵ and the aperture function is defined as

$$w(u) = \begin{cases} 1, & |u| \leq 21 \text{ cm}, \\ 0, & \text{elsewhere.} \end{cases} \quad (4)$$

Figure 9 shows that the ground-reflection model works well; the ground reflection is mostly eliminated in images from both the clean surface experiment and the cluttered surface experiment. However, the ground-reflection model is believed to be the source of the horizontal artefact near the target depth. Note that the targets are more localized in the back-projected images than in the raw gray-scale graphs.

In Figure 9, the targets at shallow depths are only seen by small bistatic apertures while the targets at deep depths are seen by bigger bistatic apertures. Thus, it may produce better images to combine responses from only small bistatic apertures, e.g., 12 cm – 36 cm wide bistatic apertures, for shallow targets and responses from more bistatic apertures, e.g., 12 cm – 72 cm wide bistatic apertures, for deeply buried targets. Figure 10 shows the 2-dimensional energy plot of the processed image of the scan region in a 20 dB scale. The energy is summed from 0 cm to 25 cm deep. For the depth from 0 cm and 8 cm, the responses from T1-R1, T1-R2, and T1-R3 bistatic pairs are coherently added, and for the depth from 8 cm to 25 cm, the responses from T1-R1, T1-R2, T1-R3, T1-R4, T2-R1, and T2-R2 bistatic pairs are coherently added. In Figure 9 (a), most targets are visible. However, in Figure 9 (b), the targets are visible, but heavily obscured by the surface clutter. The images may be improved by modifying the aperture function in Equation (4) to have the path-length dependency. In addition, Figure 9 (b) shows that we need a better clutter removal algorithms.

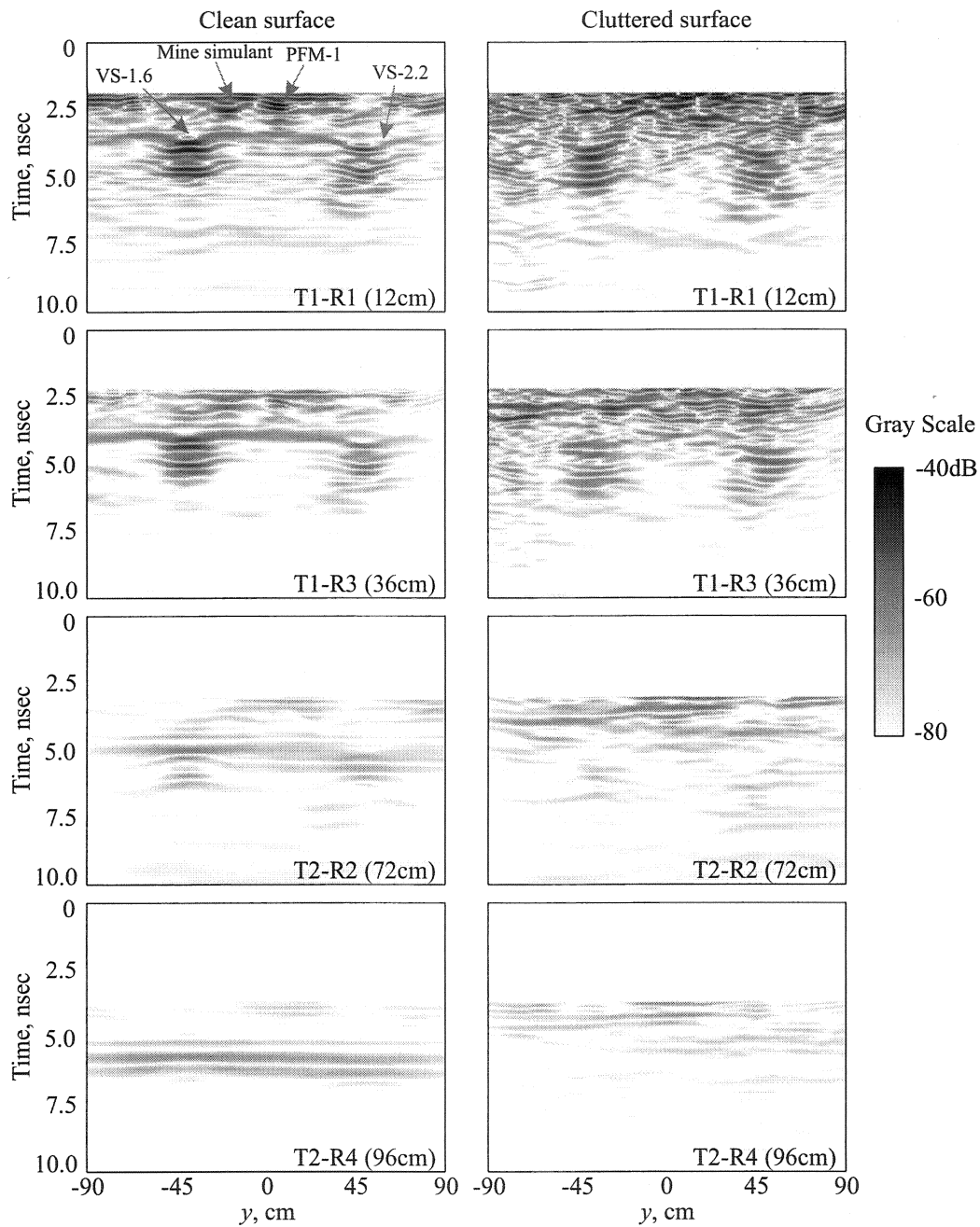


Figure 9. Back-projected images of the signal intensities obtained from 12 cm, 36 cm, 72 cm, and 96 cm wide bistatic apertures when the array is scanned over the line at $x = 0$. The images on the top row are those from the clean surface experiment, and the images on the bottom row are those from the cluttered surface experiment.

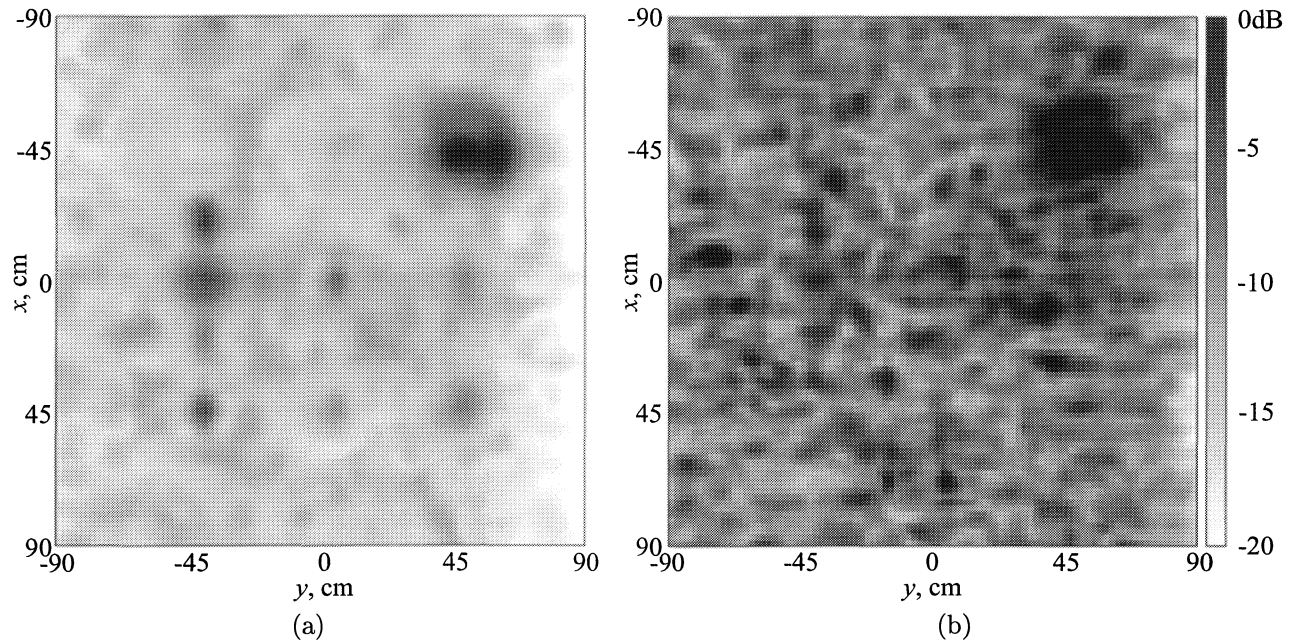


Figure 10. Back-projected images of the energy over the scan region (a) when the surface is clean and (b) when the surface is cluttered.

5. CONCLUSION

A multi-static GPR has been developed to investigate the potential of the multi-static inversion algorithms. The multi-static GPR consists of 6 resistively-loaded vee dipoles, a network analyzer, and a microwave switch matrix, and a control computer. The multi-static GPR can obtain the responses from eight elementary bistatic apertures simultaneously. These elementary bistatic apertures can be used to form various synthetic apertures. As examples, 96 cm wide, nine-element synthetic aperture and 196 cm wide, 17-element synthetic aperture were illustrated.

The operation of the multi-static GPR was demonstrated on landmine targets buried in sand with clean surface and in sand with cluttered surface. The raw data were plotted in gray scale to show that the targets have different responses to different bistatic apertures. A modified delay-sum back-projection algorithm was used to process the raw data. Most targets were seen on the back-projected images for the targets in clean sand. However, the images for the targets in cluttered sand are seen to be significantly obscured.

The experiments in the paper simulate both minimally cluttered environment and heavily cluttered environment. This set of experiments may be a good starting point to prove the efficiency of the existing and newly developed inversion algorithms.

ACKNOWLEDGMENTS

This work is supported in part by the US Army Research Office under Contract Number DAAD19-02-1-0252.

REFERENCES

1. W. R. Scott, Jr., P. D. Norville, Kangwook Kim, J. H. McClellan, and G. D. Larson, "Experimental investigation of techniques for the detection of near surface targets in cluttered media." in *Institute for Mathematics and its Applications (IMA) "Hot Topics" Workshop: Adaptive Sensing and Multimode Data Inversion*, Minneapolis, MN, June 27-30, 2004.
2. T. P. Montoya and G. S. Smith, "Resistively-loaded vee antennas for short-pulse ground penetrating radar," in *IEEE Int. Antennas Propagat. Symp. Dig.*, pp. 2068-2071, Jul. 1996.

3. T. P. Montoya and G. S. Smith, "Vee dipoles with resistive loading for short-pulse ground-penetrating radar," *Microwave Optical Tech. Lett.* **13**(3), pp. 132–137, Oct. 1996.
4. T. T. Wu and R. W. P. King, "The cylindrical antenna with nonreflecting resistive loading," *IEEE Trans. Antennas Propagat.* **AP-13**(3), pp. 369–373, May 1965. Correction: L. C. Shen and R. W. P. King, vol. 13, no. 6, p. 998, Nov. 1965.
5. Kangwook Kim and W. R. Scott, Jr., "Design and realization of a discretely loaded resistive vee dipole for ground-penetrating radars," *Radio Science, in the special section: Remote Sensing of Land Mines* **39**(4), July 2004.
6. Kangwook Kim and W. R. Scott, Jr., "A resistive linear antenna for ground-penetrating radars," in *Detection and Remediation Technologies for Mines and Minelike Targets IX, Proc. SPIE*, **5415**, pp. 359–370, April 2004.
7. Kangwook Kim and W. R. Scott, Jr., "Improved resistively-loaded vee dipole for ground-penetrating radar applications," in *2004 IEEE Int. Antennas Propagat. Symp. Dig.*, **3**, pp. 2548–2551, June 20–26, 2004.
8. Kangwook Kim and W. R. Scott, Jr., "Design of a resistively-loaded vee dipole for ultra-wideband ground-penetrating radar applications," *IEEE Trans. Antennas Propagat.*, accepted for publication.
9. Kangwook Kim and W. R. Scott, Jr., "Investigation of resistive vee antennas for a multi-static ground-penetrating radar," in *IEEE Int. Antennas Propaga. Symp.*, 2005, accepted for publication.
10. M. Soumekh, *Synthetic aperture radar signal processing with MATLAB algorithms*, A Wiley-Interscience publication, 1999.
11. J. M. Lopez-Sanchez and J. Fortuny-Guasch, "3-D radar imaging using range migration techniques," *IEEE Trans. Antennas Propagat.* **48**, pp. 728–737, May 2000.
12. L. van Kempen and H. Sahli, "Ground penetrating radar data processing: A selective survey of the state of the art literature." Technical Report IRIS-TR-0060, Vrije Universiteit Brussel, ETRO Department, 1999.
13. Agilent Technologies, "Agilent 8719D, 8720D, and 8722D Network Analyzers Data Sheet," 1998.
14. S. Oh, *Iterative Space-time domain fast multiresolution SAR imaging algorithms*. PhD thesis, Georgia Institute of Technology, Nov. 2001.
15. E. M. Johansson and J. E. Mast, "Three-dimensional ground penetrating radar imaging using synthetic aperture time-domain focusing," in *Advanced Microwave and Millimeter-Wave Detectors, Proc. SPIE*, **2275**, pp. 205–214, 1994.